DOI: 10.1002/((please add manuscript number))
Article type: Communication

Tuning Nanofillers in In-situ Prepared Polyimide Nanocomposites for High-Temperature Capacitive Energy Storage

Ding Ai, He Li, Yao Zhou, Lulu Ren, Zhubing Han, Bin Yao, Wei Zhou, Ling Zhao, Jianmei Xu and Qing Wang**

D. Ai, Prof. W. Zhou, Prof. L. Zhao, Prof. J. Xu
Faculty of Materials Science and Chemistry, China University of Geosciences, Wuhan, Hubei 430078, China
E-mail: jianmei@cug.edu.cn

D. Ai, Dr. H. Li, Dr. Y. Zhou, L. Ren, Z. Han, B. Yao, Prof. Q. Wang
Department of Materials Science and Engineering, The Pennsylvania State University, University Park, Pennsylvania 16802, USA
E-mail: wang@matse.psu.edu

Keywords: polymer nanocomposites, nanostructured inorganic fillers, capacitors, high temperature, energy density

Abstract: Modern electronics and electrical systems demand efficient operation of dielectric polymer-based capacitors at high electric fields and elevated temperatures. Here, we report the polyimide dielectric composites prepared from in-situ polymerization in the presence of inorganic nanofillers. The systematic manipulation of the dielectric constant and bandgap of the inorganic fillers, including Al_2O_3, HfO_2, TiO_2 and boron nitride nanosheets, reveals the dominant role of the bandgap of the fillers in determining and improving the high-temperature capacitive performance of the polymer composites, which is very different from the design principle of the dielectric polymer composites operating at ambient temperature. The Al_2O_3 and HfO_2 based polyimide composites with concomitantly large bandgap and moderate dielectric constants exhibit substantially improvement in the breakdown strength, discharged energy density and charge-discharge efficiency when compared to the state-of-the-art dielectric polymers. The work provides a design paradigm for high-performance dielectric polymer nanocomposites for electrical energy storage at elevated temperatures.

Dielectric capacitors possess the highest power density among the energy storage devices and are one of the major enabling technologies for advanced electronics and electrical power systems.[1−3] In particular, capacitors with high operating temperatures are of critical importance for next-generation automotive and aerospace power systems. In electric vehicles, power inverters convert direct current from batteries to alternating current at the frequency required to control the electric motor. Because of close proximity to the engine and the ever-increasing demand for power capability, it requires that capacitors, the essential element of power inverters, operate at a temperature of 140 °C or above.[4,5] While dielectric ceramics are traditional materials for high-temperature capacitors,[6] they are severely limited by scalability, weight, fracture toughness and breakdown strength in comparison to their polymer counterparts.[7−17] Biaxially oriented polypropylene film (BOPP), the state-of-the-art commercially available polymer dielectric, however, shows largely degraded high-field dielectric properties when operating at temperatures above 100 ^{o}C.[18]

To address these imperative needs, a variety of well-established engineering polymers, including polycarbonate (PC), polyimide (PI), polyetherimides (PEI) and poly(ether ether ketone) (PEEK), have been exploited as high-temperature dielectric materials.[19−25] As these aromatic polymers have high glass transition temperatures (T_g) and excellent thermal stability, it is anticipated that the engineering polymers would retain electromechanical properties and thus dielectric stability at high temperatures. However, when subjected to high applied fields, the engineering polymers exhibit limited working temperatures that are much lower than their T_gs.[19,20] More recently, inorganic fillers represented by boron nitride nanosheets (BNNSs) have been incorporated into crosslinked divinyltetramethyldisiloxane-bis(benzocyclobutene) (*c*-BCB) to yield the dielectric polymer composites capable of operating efficiently at high temperatures, e.g. 150 ^{o}C.[26−29] Herein, we describe the high-temperature dielectric properties and capacitive performance of the PI-based polymer nanocomposites prepared via in-situ polycondensation. Compared with *c*-BCB, PI possesses the inherent advantages including much better processability, considerably lower

cost, and greater mechanical strength and flexibility, which potentially offers a scalable route toward robust high-temperature dielectric materials.[30,31] The investigation of the polymer composites containing the inorganic nanofillers with systematically varied dielectric constants (*K*) and bandgap (ΔE), including aluminium oxide (Al_2O_3) with a *K* of 9.5 and a ΔE of 8.6 eV, hafnium dioxide (HfO_2) with a *K* of 25 and a ΔE of 5.8 eV, titanium dioxide (TiO_2) with a *K* of 110 and a ΔE of 3.5 eV, and BNNS with a *K* of 4 and a ΔE of 5.97 eV,[26,32–34] would provide experimental guidelines for the design of high-performance high-temperature dielectric polymer composites.

As shown in Figure 1, pyromellitic dianhydride (PMDA), and 4, 4-diaminodiphenyl ether (4, 4'-ODA) were condensed in the presence of inorganic nanofillers including Al_2O_3, HfO_2, TiO_2 and BNNS. The in-situ synthesis of the PI composites starts from the mixture of ODA and the nanofiller suspension toward the preparation of the precursor of PI - poly(amic aicid) (PAA), which has been found to be effective in disrupting nanofillers agglomeration and thus yield the composites with uniform filler dispersion and excellent dielectric properties.[35] The formation of PAA and subsequent thermal imidization were monitored by using attenuated total reflectance-Fourier transform infrared (ATR-FTIR) spectroscopy (Figure S1 Supporting Information). The absence of 3252 and 1624 cm^{-1} absorption bands arising from N-H and C=O stretching of PAA, respectively, and the appearance of new peaks at 1775 cm^{-1} (C=O asymmetric stretching), 1720 cm^{-1} (C=O symmetric stretching), 1366 cm^{-1} (C-N stretching) and 723 cm^{-1} (C=O bending) indicate the successful conversion of PAA to PI upon thermal curing. The presence of the nanofillers in the in-situ prepared nanocomposites has been manifested by the FTIR spectra (Figure S1 Supporting Information) and cross-sectional scanning electron microscopic (SEM) images (Figure S2 Supporting Information). Homogeneous dispersion of the nanofillers in the PI matrix prepared by the in-situ polycondensation is evidenced in SEM. For the purpose of comparison, the dielectric properties and capacitive performance of pristine PI films were evaluated along with the PI nanocomposites.

As summarized in Figure 2A, the *K* of the nanocomposites is enhanced upon the incorporation of the nanofillers, *e.g.*, from 3.33 for PI to 3.46 of PI-BNNS, 3.58 of PI-Al_2O_3, 3.76 of PI-HfO_2 and 4.02 of PI-TiO_2 with 5 vol% filler content measured at 25 °C and 1 kHz, and increases gradually with the filler content. The increasing *K* is attributable to higher *K* values of the fillers relative to that of PI matrix. As expected, TiO_2 with the highest *K* among the nanofillers investigated herein gives rise to the largest *K* of the nanocomposites, whereas the PI-BNNS composites possess the lowest *K* owing to the smallest *K* of BNNS. It is found that the experimental *K* values of the PI-Al_2O_3, PI-HfO_2 and PI-TiO_2 composites agree well with the effective *K* calculated by using the Lichtenecker model (Eq. 1)[36] which is a widely used empirical model to determine the *K* of dielectric composites where the spherical particles were randomly dispersed in the matrix. The fitting results for the PI-Al_2O_3, PI-HfO_2 and PI-TiO_2 composites by using other theoretical models are shown in Figure S3 Supporting Information.[37] For PI-BNNS, the experimental *K* was fitted well by using the Polder-Van Santen (PVS) formalism (Eq. 2)[38]

$$\varepsilon_{\text{eff}} = e^{f_a \ln \varepsilon_a + (1-f_a)\ln \varepsilon_b} \quad \text{(Eq. 1)}$$

$$\varepsilon_{\text{eff}} = \varepsilon_b + \frac{f_a(\varepsilon_a - \varepsilon_b)}{3} \sum_{j=x,y,z} \frac{\varepsilon_{\text{eff}}}{\varepsilon_{\text{eff}} + N_j(\varepsilon_a - \varepsilon_{\text{eff}})} \quad \text{(Eq. 2)}$$

where ε_{eff}, ε_b and ε_a are the *K* of the composite, matrix and nanofiller, respectively, f_a is the volume fraction of the nanofiller and N_j represents the depolarization factors (Eq. S1 Supporting Information). All the PI-based composites exhibit low dielectric loss (<0.5%) as shown in Figure 2A. In addition, dielectric spectroscopy reveals that *K* and dielectric loss of the PI composites are considerably stable with respect to temperature ranging from 25 to 200 °C and frequency ranging from 100 Hz to 1 MHz, which retain the unique features of PI matrix (Figures S4 and S5 Supporting Information).

The breakdown strength (E_b) of the polymer nanocomposites at 150 °C is analyzed with a two-parameter Weibull statistic distribution function described as:

$$P(E) = 1 - \exp(-(E/E_b)^{\beta}) \quad \text{(Eq. 3)}$$

where $P(E)$ is the cumulative probability of electric failure, E is the measured breakdown field, Weibull breakdown strength E_b represents the field strength at the cumulative failure probability of 63.2%, β is the shape parameter evaluating the scatter of the breakdown data. At least 15 measurements were made for each Weibull fitting. Notably, as summarized in Figure 2B and Figure S7 Supporting Information, the E_b of the PI nanocomposites increases from 314 MV m^{-1} of PI with the incorporation of the nanofillers and is maximized to 340 MV m^{-1} at 1 vol% TiO_2, 397 MV m^{-1} at 5 vol% HfO_2, 422 MV m^{-1} at 7 vol% Al_2O_3, and 418 MV m^{-1} at 5 vol% BNNS. This is in sharp contrast to the typical dielectric polymer composites with high-K inclusions whose E_b is always largely reduced when compared to that of pristine polymers.[8,39,40] It is found that the systematic enhancement in the E_b of the PI nanocomposites coincides with the increasing trend of ΔE of the nanofillers as summarized in Figure S8 Supporting Information. Al_2O_3 has the largest ΔE among the fillers and results in the highest E_b of the composites, while TiO_2 with the lowest ΔE leads to the smallest improvement in E_b of the resulting composites. Apparently, the nanofillers with higher ΔE are more efficient in acting as barriers against charge injection from electrodes and the growth of electrical trees in dielectrics at elevated temperatures. In addition, compared to Al_2O_3 and BNNS, TiO_2 has the largest contrast in K with PI matrix, which may create more significant distortion of local fields and thus yield a reduced E_b in the composites at high filler contents.[8, 41] Different from the PI composites with BNNS, Al_2O_3 and HfO_2 fillers, the E_b of the PI-TiO_2 composites decrease rapidly with increasing filler concentration. The initial increase in the E_b of the PI-TiO_2 composites could be attributed to the contribution of the interfaces between the nanoparticles and the polymer, which serves as effective electron scatters and trapping centers to impede charge conduction in the composites.[16,17] As shown in Figures S6 and S7, further increase of the filler concentration results in decreased E_b,[42,43] which matches the change of the electrical conductivity of the composites as discussed below.

Representative electric displacement-electric field (*D*-*E*) loops of the PI-nanocomposites measured at 150 °C and 200 MV m^{-1}, which is the working condition of the power inverters in electric vehicles,[44] are displayed in Figure S12 Supporting Information, in which the integral of the area bounded by the upper line and the y-axis represents the dischargeable energy density (U_e) and the area enclosed by the upper and bottom lines stands for energy loss (U_l). The nanocomposites with high-*K* nanofillers display correspondingly large values of *D*, *i.e.* the largest *D* of 0.0080 - 0.0084 C m^{-2} found in the PI-HfO_2 and PI-TiO_2 composites. On the other hand, it is seen that the PI-BNNS, PI-Al_2O_3 and PI-HfO_2 composites with large ΔE fillers present the lowest U_l, and consequently, the highest charge-discharge efficiency ($\eta = U_e/(U_e + U_l)$), *i.e.* 93.3% - 95.8%, which is much greater than neat PI , *i.e.* 79.7%. Figure 2C summarizes the U_e and η of the composites with the optimized filler content measured at 150 °C and under their respective E_b. Clearly, the PI-composites significantly outperform PI matrix in both U_e and η. For instance, at an applied field of 250 MV m^{-1}, PI exhibits the maximum U_e of 0.82 J cm^{-3} and a η of 55.7%, whereas the respective U_e and η are 1.12 J cm^{-3} and 93.7% for PI-Al_2O_3, 1.21 J cm^{-3} and 91.0% for PI-HfO_2, 1.08 J cm^{-3} and 91.8% for PI-BNNS, and 1.11 J cm^{-3} and 81.8% for PI-TiO_2. As compared in Figure 2D, the capacitive performance of the PI-composites under different applied fields critically depends on the *K* and ΔE of the fillers. Although TiO_2 has the highest *K* of 110 and the largest *D* (e.g. 0.0084 C m^{-2} @ 200 MV m^{-1}) among the fillers, it fails to yield a superior U_e at high applied fields (*i.e.* >50 MV m^{-1}). Its lowest ΔE of 3.5 eV gives the largest U_l that can overshadow any other advantages gained from high *K*. At an applied field of 200 MV m^{-1}, HfO_2, which has a relatively high *K* of 25 and a moderately large ΔE of 5.8 eV, gives rise to the PI composite with the highest U_e. On the other hand, the PI-BNNS composite has the lowest U_e as a direct consequence of its smallest *K* of 4 of BNNS. At high applied fields, it is found that ΔE of the fillers vitally determines the capacitive performance of the composites. Al_2O_3, which has the largest ΔE of 8.6 eV and a reasonably large *K* of 9.5, yields the best composite operating at 350 MV m^{-1} and 150 °C. The U_e of the PI-Al_2O_3 and PI-HfO_2

composites surpasses that of *c*-BCB/BNNSs and rival the newly developed high-temperature dielectric polymer nanocomposites.[26,33] Moreover, compared to the BNNS-filled polymer composites, the PI-Al_2O_3 and PI-HfO_2 composites have much improved scalability as Al_2O_3 and HfO_2 nanofillers either are commercially available or can be prepared readily in large scales. On the contrary, BNNSs are typically prepared via solution exfoliation under sonication, which is a low-yield (<10%) and time-consuming (~48 hrs) process.[45] Comparatively, BOPP operating at 70 °C and 200 MV m^{-1} has a U_e of 0.4 J cm^{-3} and a η of 96%.[28] These results indicate that, by substitute BOPP with the PI-Al_2O_3 and PI-HfO_2 nanocomposites in the power inverters, the secondary cooling system in electric vehicles could be eliminated to improve volume and fuel efficiency and enhance reliability and performance of power systems. In addition, improved U_e enables the reduction in weight and size of electrical energy storage and power conditioning systems. Currently, capacitors represent up to 23% of the inverter weight and up to 35-40% of the inverter volume. It is estimated that a 100% increase in U_e corresponds to more than 17% reduction in the inverter size.[46] To evaluate the stability of the PI composites, charge-discharge cycling has been conducted at 150 °C under an applied filed of 200 MV m^{-1}. Remarkably, as shown in Figure S16 Supporting Information, no sign of degradation in the discharged energy density and the charge–discharge efficiency has been detected in the PI composites over 25,000 cycles. SEM shown in Figure S17 Supporting Information confirms the structure durability of the composites after cycling.

It is recognized that electrical conduction is the major loss mechanism of dielectrics at high electric fields.[18,33,47] Indeed, as shown in Figure 3A, the conduction loss of PI and the PI composites increase exponentially with the applied electric fields, which accounts for the deteriorating U_e and η observed at high fields. It is clearly evident from Figure 3B and Figure S18 Supporting Information that significant reductions in the electrical conductivity have been achieved upon the introduction of the nanofillers in PI matrix, which is particularly prominent at high temperatures. At 25 °C, the volume conductivity of neat PI measured at 100 MV m^{-1} is reduced by 33.4%, 47.0%, 53.2% and 72.6% with the incorporation of TiO_2, HfO_2, BNNS, and Al_2O_3,

respectively. While at 150 °C, the corresponding decreases in the conductivity are much more pronounced, *i.e.* 41.1%, 83.2%, 89.9% and 93.9%, respectively. It is noteworthy that the magnitude of reduction follows the trend of increasing ΔE of the fillers from TiO_2, HfO_2, BNNS to Al_2O_3. Consequently, at high fields, the Al_2O_3 composite presents the lowest loss and the best η, while the TiO_2 composite has the highest loss and the lowest η as shown in Fig. 2D. In addition, the exponential increase of current density (J) over the electric field is shown in Figure 3C, in which J is given as:[48]

$$J = 2nedv * \exp[(-U / K_b T)] * \sinh(deE / 2K_b T) \quad \text{(Eq. 4)}$$

where U is the activation energy, d is the hopping distance, and v is the attempt-to-escape frequency, n is the carrier density, K_b is the Boltzmann constant, T is the temperature and e represents the electric charge. Eq. 4 can be simplified as follows:

$$J = J_0 * \sinh(\alpha * E) \quad \text{(Eq. 5)}$$

where J_0 and α are two lumped parameters. The fitting of the experimental J data of the PI nanocomposites to Eq.5 suggests that hopping conduction is dominant in the nanocomposites at high electric fields. The hopping distance d can be calculated from the slopes of the fitting curves. For PI, the d is about 1.83 nm at 150 °C, which is decreased to 1.69, 1.41, 1.38 and 1.25 nm of the PI-TiO_2, PI-HfO_2, PI-BNNS and PI-Al_2O_3 nanocomposites, respectively. The decrease in the d denotes the increase in the trap depth, which is naturally responsible for the reduced conduction current and lowered dielectric loss.[33] Accordingly, the shortest d of the PI-Al_2O_3 composites correlates well with the lowest high-field conductivity and the smallest U_l. Note that the decrease in the d of the PI nanocomposites also follows the increasing trend of ΔE of the nanofillers, which is consistent with the E_b results (Figure S7 Supporting Information).

To better understand the dependence of leakage current density on the ΔE of the fillers, we simulated the current density distribution as a function of the filler content and applied field at 150 °C according to the hopping conduction model. As shown in Figure 4, in concert with the

experimental results, the simulations indicate that the PI nanocomposites consisting of Al_2O_3 and HfO_2 filler with larger ΔE exhibit much lower leakage current than the PI-TiO_2 composite. The volume resistivity of the PI nanocomposites versus the volume fractions of nanofillers at 200 MV m^{-1} has been summarized in Figure S20, S21 and S22 Supporting Information. The volume resistivity of the composites increases with the filler content and then decreases at a certain filler content, which is consistent with the trend of E_b results. High concentrations of the fillers are prone to structure defects and filler agglomeration and have better connectivity, thus leading to increased leakage current and the corresponding reduction in volume resistivity and breakdown strength.[49] In addition, the thermally stimulated depolarization current (TSDC) measurements have been conducted to assess the charge trapping characteristics of the materials. As can be seen in Figure 3D, the peak located at a low temperature region stems from dipole polarization, while the high temperature peak is associated with the space charge polarization by trapping of charge carriers in deeper traps.[50] The much increased intensity of the peaks in the PI composites relative to those of PI implies that more charges are trapped upon the incorporation of nanofillers. Moreover, the shift of the high temperature peak toward high temperatures (e.g., >200 ^oC) from PI to the PI nanocomposites is indicative of the formation of deeper traps in the composites.[51] These results offer direct insights in the origins of the suppressed conduction loss and improved η observed in the PI nanocomposites.

In summary, we have prepared a series of the PI-based polymer nanocomposites containing the inorganic nanofillers with systematically varied K and ΔE. Different from the typical dielectric composites whose E_b is reduced with the incorporation of high-K inclusions, the PI-composites exhibit much improved E_b in comparison to pristine PI. In contrast to the dielectric composites designed for operating at weak fields and room temperature, in which K of the fillers plays a crucial role in determining the dielectric performance, it is conclusively demonstrated that ΔE of the fillers dominates the high-temperature capacitive performance of the polymer composites at high fields.

The addition of the inorganic fillers with large ΔE significantly reduces conduction current, which yields the dielectric composites with high U_e and great η at high fields and elevated temperatures. The synergistic combination of a large ΔE and a moderate K in Al_2O_3 and HfO_2 gives rise to the corresponding composites with superior capacitive performance than the state-of-the-art dielectric polymers and *c*-BCB/BNNS composite at elevated temperatures. Furthermore, the PI-Al_2O_3 and PI-HfO_2 composites have greater scalability when compared to the current high-temperature dielectric polymer composites which are mostly based on *c*-BCB matrix. This work reveals the pronounced impact of inorganic nanofillers on high-temperature capacitive performance of the polymer composites and sheds light on the rational design of scalable dielectric polymer composites for applications in electric energy storage under extreme environments.

Supporting Information
Supporting Information is available from the Wiley Online Library or from the author.

Acknowledgements
D.A. acknowledges the support from the China Scholarship Council (CSC).

Received: ((will be filled in by the editorial staff))
Revised: ((will be filled in by the editorial staff))
Published online: ((will be filled in by the editorial staff))

References

[1] W. J. Sarjeant, J. Zirnheld, F. W. MacDougall, *IEEE Trans. Plasma Sci.* **1998**, *26*, 1368.

[2] Q. Tan, P. Irwin, Y. Cao, *IEEJ Trans. Fundam. Mater.* **2006**, *126*, 1152.

[3] B. Chu, X. Zhou, K. Ren, B. Neese, M. Lin, Q. Wang, F. Bauer, Q. M. Zhang, *Science* **2006**, *313*, 334.

[4] R. W. Johnson, J. L. Evans, P. Jacobsen, J. R. Thompson, M. Christopher, *IEEE Trans. Electron. Packag. Manuf.* **2004**, *27*, 164.

[5] J. Watson, G. Castro, *Analog Dialog* **2012**, *46*, 1.

[6] H. Palneedi, M. Peddigari, G.-T. Hwang, D.-Y. Jeong, J. Ryu, *Adv. Funct. Mater.* **2018**, *28*, 1803665.

[7] Z. Pan, L. Yao, J. Zhai, X. Yao, H. Chen, *Adv. Mater.* **2018**, *30*, 1705662.

[8] H. Li, F. Liu, B. Fan, D. Ai, Z. Peng, Q. Wang, *Small Methods* **2018**, *2*, 1700399.

[9] Z. M. Dang, J. K. Yuan, S. H. Yao, R. J. Liao, *Adv. Mater.* **2013**, *25*, 6334.

[10] Y. Wang, L. Wang, Q. Yuan, J. Chen, Y. Niu, X. Xu, Y. Cheng, B. Yao, Q. Wang, H. Wang, *Nano Energy* **2018**, *44*, 364.

[11] S. Luo, J. Yu, S. Yu, R. Sun, L. Cao, W. H. Liao, C. P. Wong, *Adv. Energy Mater.* **2019**, *9*, 1803204.

[12] X. Huang, P. Jiang, *Adv. Mater.* **2015**, *27*, 546.

[13] L. Zhu, *J. Phys. Chem. Lett.* **2014**, *5*, 3677.

[14] Y. Zhu, Y. Zhu, X. Huang, J. Chen, Q. Li, J. He, P. Jiang, *Adv. Energy Mater.* **2019**, *9*, 1901826.

[15] X. Zhang, J. Jiang, Z. Shen, Z. Dan, M. Li, Y. Lin, C. W. Nan, L. Q. Chen, Y. Shen, *Adv. Mater.* **2018**, *30*, 1707269.

[16] Y. Wang, J. Cui, Q. Yuan, Y. Niu, Y. Bai, H. Wang, *Adv. Mater.* **2015**, *27*, 6658.

[17] J. Chen, Y. Wang, Q. Yuan, X. Xu, Y. Niu, Q. Wang, H. Wang, *Nano Energy* **2018**, *54*, 288.

[18] J. S. Ho, T. R. Jow, *IEEE Trans. Dielectr. Electr. Insul.* **2012**, *19*, 990.

[19] Q. Li, F. Z. Yao, Y. Liu, G. Zhang, H. Wang, Q. Wang, *Annu. Rev. Mater. Res.* **2018**, *48*, 219.

[20] J. S. Ho, S. G. Greenbaum, *ACS Appl. Mater. Interfaces* **2018**, *10*, 29189.

[21] B. Fan, F. Liu, G. Yang, H. Li, G. Zhang, S. Jiang, Q. Wang, *IET Nanodielectr.* **2018**, *1*, 32.

[22] W. Xu, J. Liu, T. Chen, X. Jiang, X. Qian, Y. Zhang, Z. Jiang, Y. Zhang, *Small* **2019**, *15*, 1901582.

[23] J. Pan, K. Li, J. Li, T. Hsu, Q. Wang, *Appl. Phys. Lett.* **2009**, *95*, 022902.

[24] J. Pan, K. Li, S. Chuayprakong, T. Hsu, Q. Wang, *ACS Appl. Mater. Interfaces* **2010**, *2*, 1286.

[25] Z. Zhang, D. H. Wang, M. H. Litt, L. S. Tan, L. Zhu, *Angew. Chem. Int. Ed.* **2018**, *57*, 1528.

[26] Q. Li, L. Chen, M. R. Gadinski, S. Zhang, G. Zhang, H. U. Li, E. Iagodkine, A. Haque, L. Q. Chen, T. N. Jackson, Q. Wang, *Nature* **2015**, *523*, 576.

[27] A. Azizi, M. R. Gadinski, Q. Li, M. A. AlSaud, J. Wang, Y. Wang, B. Wang, F. Liu, L. Q. Chen, N. Alem, Q. Wang, *Adv. Mater.* **2017**, *29*, 1701864.

[28] Y. Zhou, Q. Li, B. Dang, Y. Yang, T. Shao, H. Li, J. Hu, R. Zeng, J. He, Q. Wang, *Adv. Mater.* **2018**, *30*, 1805672.

[29] Q. Li, F. Liu, T. Yang, M. R. Gadinski, G. Zhang, L. Q. Chen, Q. Wang, *Proc. Natl. Acad. Sci. USA* **2016**, *113*, 9995.

[30] Q. G. Chi, J. Sun, C. H. Zhang, G. Liu, J. Q. Lin, Y. N. Wang, X. Wang, Q. Q. Lei, *J. Mater. Chem. C* **2014**, *2*, 172.

[31] V. A. Bershtein, L. M. Egorova, P. N. Yakushev, P. Pissis, P. Sysel, L. Brozova, *J. Polym. Sci. Polym. Phys.* **2002**, *40*, 1056.

[32] J. Robertson, *Eur. Phys. J. Appl. Phys.* **2004**, *28*, 265.

[33] H. Li, D. Ai, L. Ren, B. Yao, Z. Han, Z. Shen, J. Wang, L. Q. Chen, Q. Wang, *Adv. Mater.* **2019**, *31*, 1900875.

[34] F. Liu, Q. Li, Z. Li, Y. Liu, L. Dong, C. Xiong, Q. Wang, *Comp. Sci. Tech.* **2017**, *142*, 139.

[35] Z. M. Dang, Y. Q. Lin, H. P. Xu, C. Y. Shi, S. T. Li, J. Bai, *Adv. Funct. Mater.* **2008**, *18*, 1509.

[36] S. Luo, Y. Shen, S. Yu, Y. Wan, W. H. Liao, R. Sun, C. P. Wong, *Energy Environ. Sci.* **2017**, *10*, 137.

[37] T. Zakri, J. P. Laurent, M. Vauclin, *J. Phys. D: Appl. Phys.* **1998**, *31*, 1589.

[38] N. Guo, S. A. DiBenedetto, P. Tewari, M. T. Lanagan, M. A. Ratner, T. J. Marks, *Chem. Mater.* **2010**, *22*, 1567.

[39] H. Luo, X. Zhou, C. Ellingford, Y. Zhang, S. Chen, K. Zhou, D. Zhang, C. R. Bowen, C. Wan, *Chem. Soc. Rev*. **2019**, *48*, 4424.

[40] J. Y. Li, L. Zhang, S. Ducharme, *Appl. Phys. Lett.* **2007**, *90*, 132901.

[41] D. Q. Tan, *Adv. Funct. Mater.* **2019**, 1808567.

[42] X. Zhang, Y. Shen, B. Xu, Q. Zhang, L. Gu, J. Jiang, J. Ma, Y. Lin, C. W. Nan, *Adv. Mater.* **2016**, *28*, 2055.

[43] H. Li, L. Ren, D. Ai, Z. Han, Y. Liu, B. Yao, Q. Wang, *InfoMat*. **2020**, DOI: 10.1002/inf2.12043

[44] D. Montanari, K. Saarinen, F. Scagliarini, D. Zeidler, M. Niskala, C. Nender, *Proc CARTS USA* **2009**, 23.

[45] J. N. Coleman, *et al Science* **2011**, *331*, 568.

[46] K. Bennion, M. Thornton, *Presented at SAE World Cong., Detroit, MI, SAE Tech. Pap.* **2010**, 01-0836.

[47] Z. H. Shen, J. J. Wang, J. Y. Jiang, Y. H. Lin, C. W. Nan, L. Q. Chen, Y. Shen, *Adv. Energy Mater.* **2018**, *8*, 1800509.

[48] V. Ambegaokar, B. I. Halperin, J. S. Langer, *Phys. Rev. B* **1971**, *4*, 2612.

[49] M. N. Almadhoun, U. S. Bhansali, H. N. Alshareef, *J. Mater. Chem.* **2012**, *22*, 11196.

[50] T. Tanaka, S. Hirabayashi, K. Shibayama, *J. Appl. Phys.* **1978**, *49*, 784.

[51] H. Lu, J. Lin, W. Yang, L. Liu, Y. Wang, G. Chen, W. Huang, *J. Appl. Polym. Sci.* **2017**, *134*, 45101.

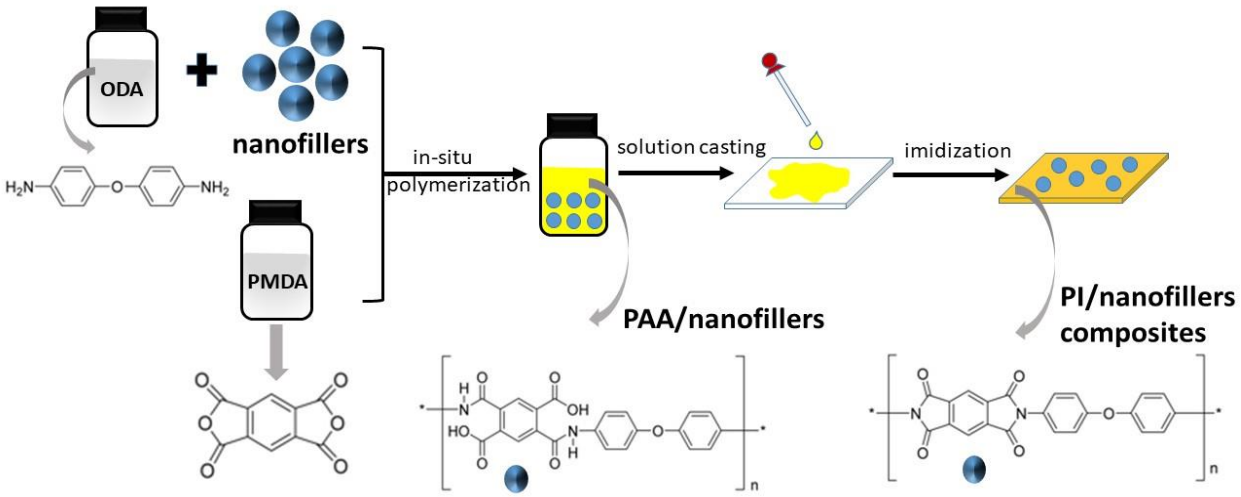

Figure 1. Schematic of the in-situ preparation of the PI-based polymer nanocomposites.

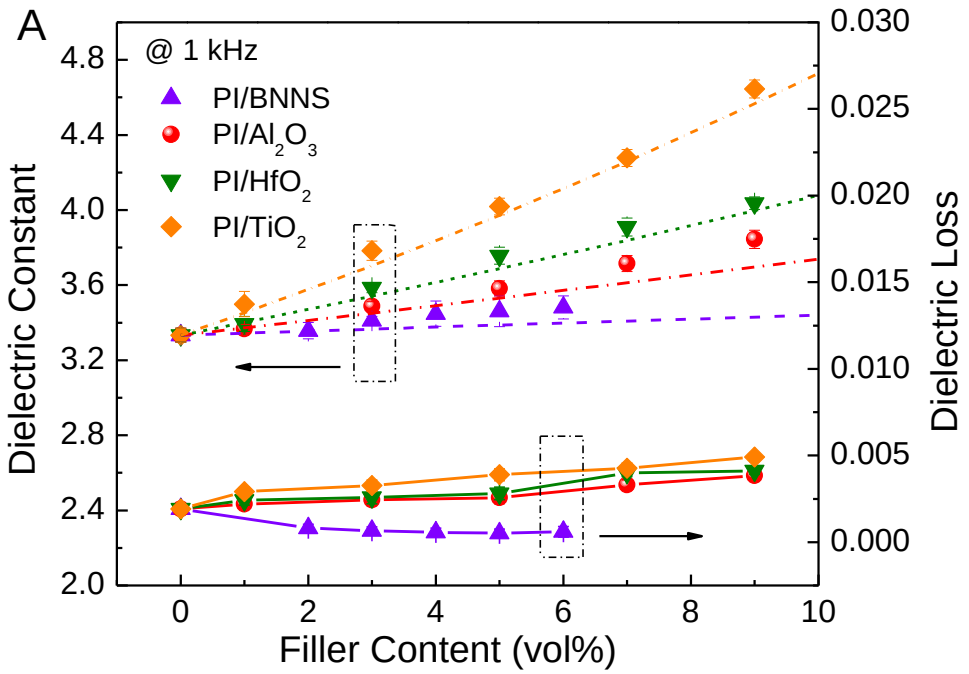
A
@ 1 kHz
PI/BNNS
PI/Al2O3
PI/HfO2
PI/TiO2
Dielectric Constant
Dielectric Loss
Filler Content (vol%)
4.8
4.4
4.0
3.6
3.2
2.8
2.4
2.0
0.030
0.025
0.020
0.015
0.010
0.005
0.000
0
2
4
6
8
10

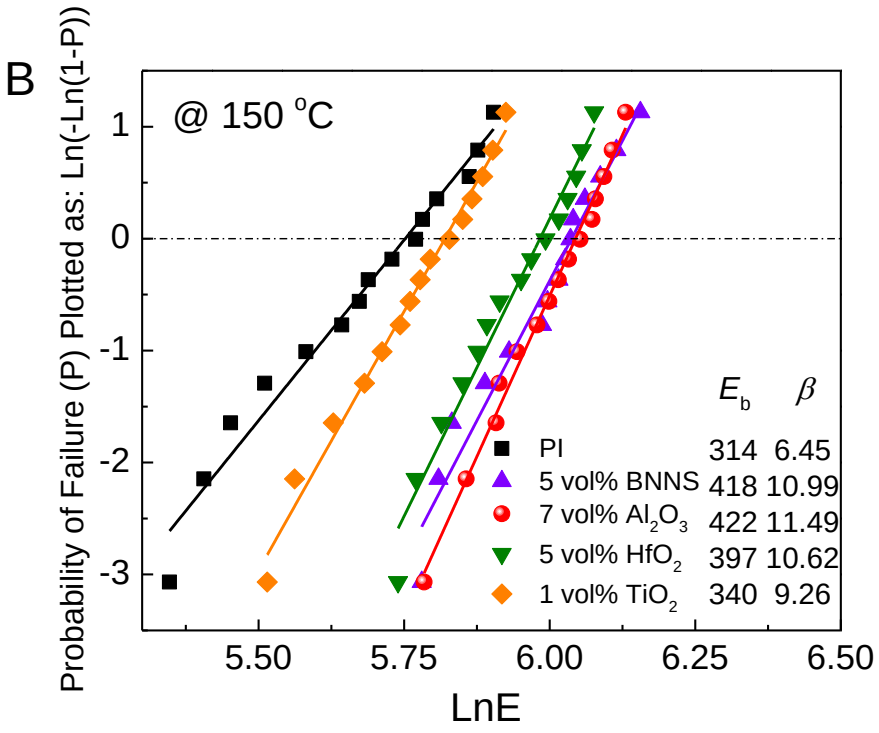
B
@ 150 °C
Probability of Failure (P) Plotted as: Ln(-Ln(1-P))
LnE
Eb β
PI 314 6.45
5 vol% BNNS 418 10.99
7 vol% Al2O3 422 11.49
5 vol% HfO2 397 10.62
1 vol% TiO2 340 9.26
1
0
-1
-2
-3
5.50
5.75
6.00
6.25
6.50

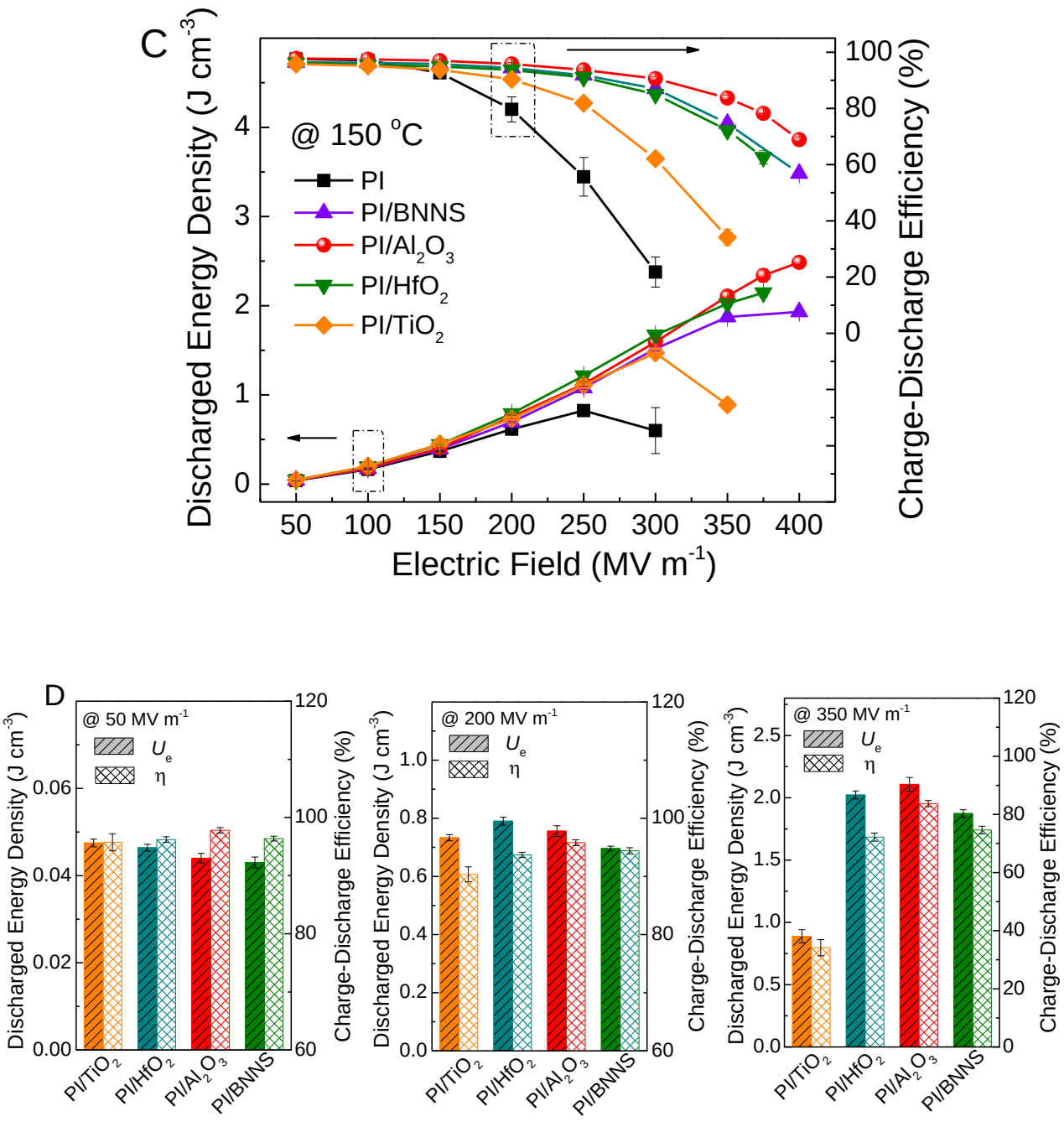

Figure 2. A) Dielectric constant and loss of the PI nanocomposites as a function of filler content at 25 °C and 1 kHz. The dash lines represent the calculated effective dielectric constant. **B)** Weibull breakdown strength of PI and the PI nanocomposites with the optimized filler contents measured at 150 °C. **C)** Discharged energy density and charge-discharge efficiency of PI and the PI nanocomposites with 5 vol% BNNS, 7 vol% Al_2O_3, 5 vol% HfO_2 and 1 vol% TiO_2 at 150 °C. **D)** Comparison of the discharged energy density and charge-discharge efficiency of the PI nanocomposites at 150 °C under different electric fields.

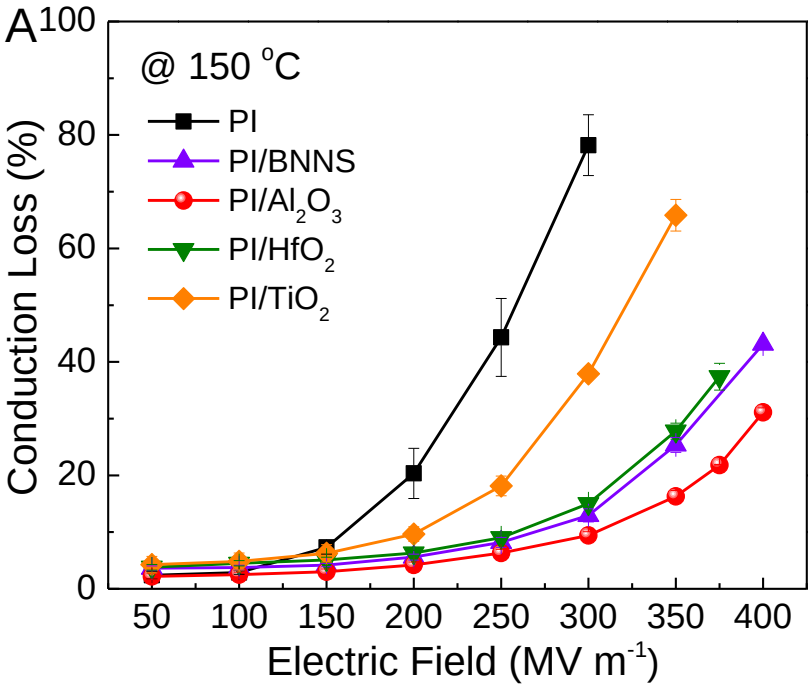
A
@ 150 °C
PI
PI/BNNS
PI/Al2O3
PI/HfO2
PI/TiO2
Conduction Loss (%)
0
20
40
60
80
100
50
100
150
200
250
300
350
400
Electric Field (MV m-1)

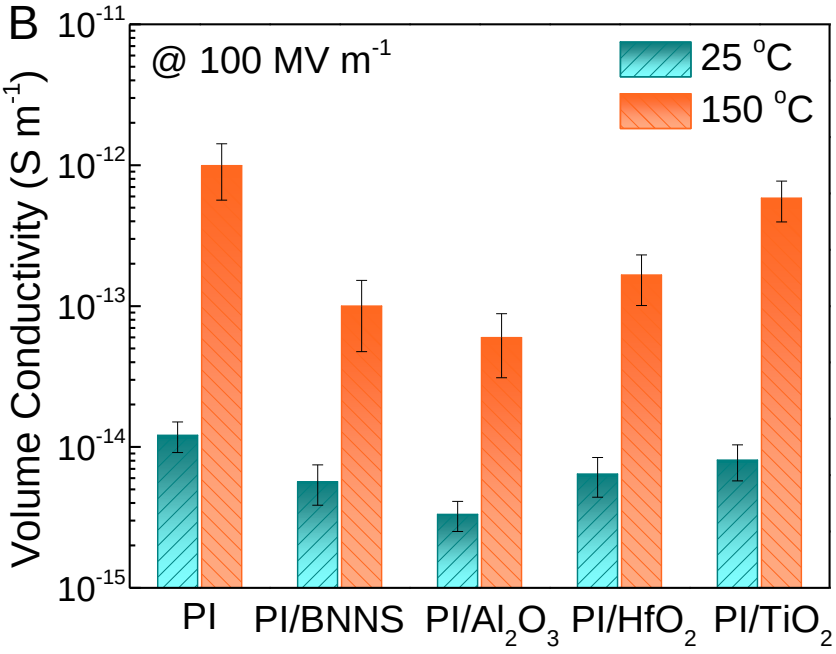
B
@ 100 MV m-1
25 °C
150 °C
Volume Conductivity (S m-1)
10-11
10-12
10-13
10-14
10-15
PI
PI/BNNS
PI/Al2O3
PI/HfO2
PI/TiO2

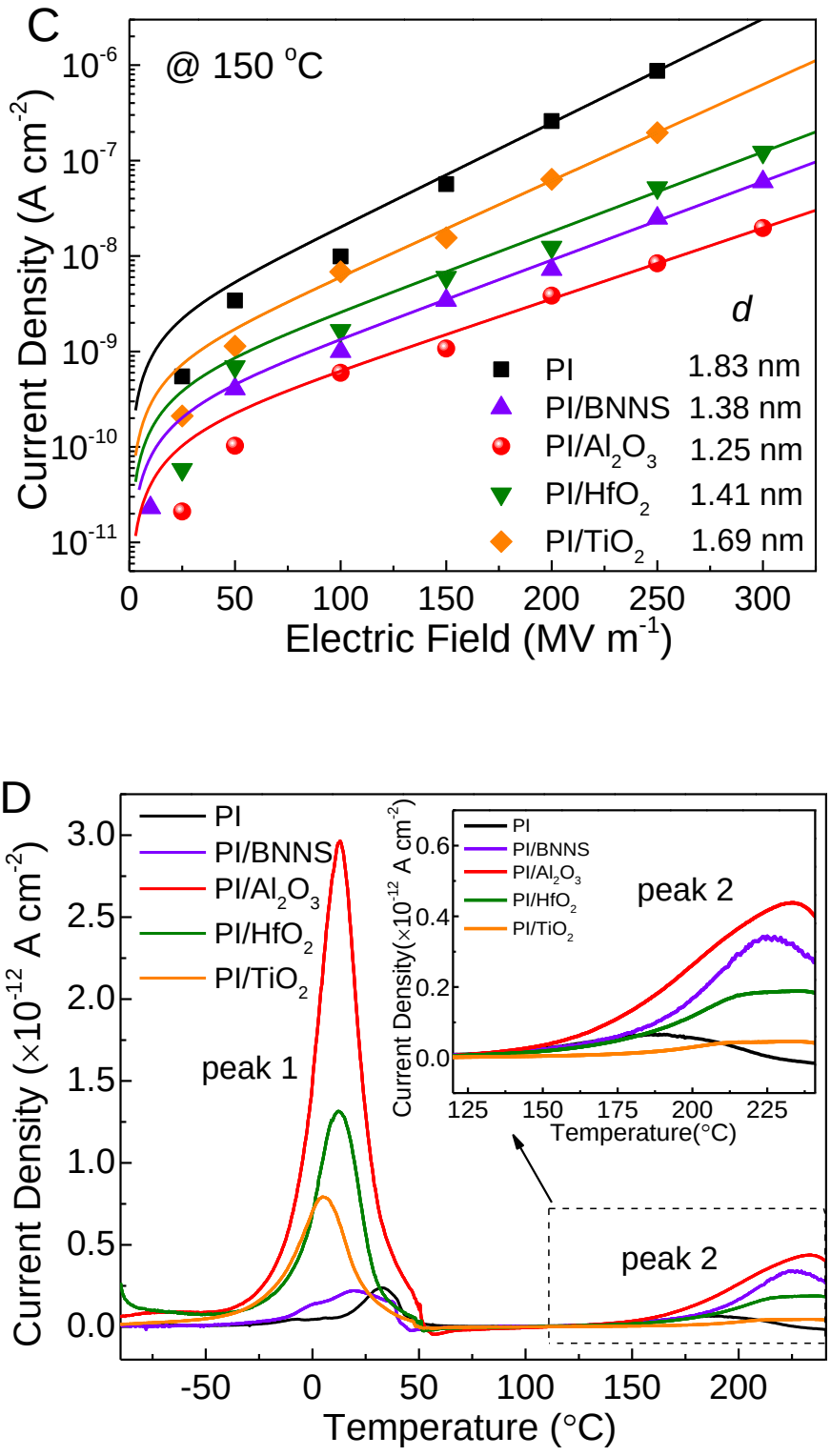

Figure 3. A) Conduction loss of PI and the PI nanocomposites with 5 vol% BNNS, 7 vol% Al_2O_3, 5 vol% HfO_2 and 1 vol% TiO_2 at 150 °C as a function of the applied field at 150 °C. **B)** Volume conductivity under 100 MV m^{-1} of PI and the PI nanocomposites at 25 °C and 150 °C. **C)** Current density of PI and the PI nanocomposites as a function of electric field at 150 °C. Solid curves represent the curve fits of Eq. 5. **D)** Thermally stimulated depolarization current (TSDC) spectra of PI and the PI nanocomposites.

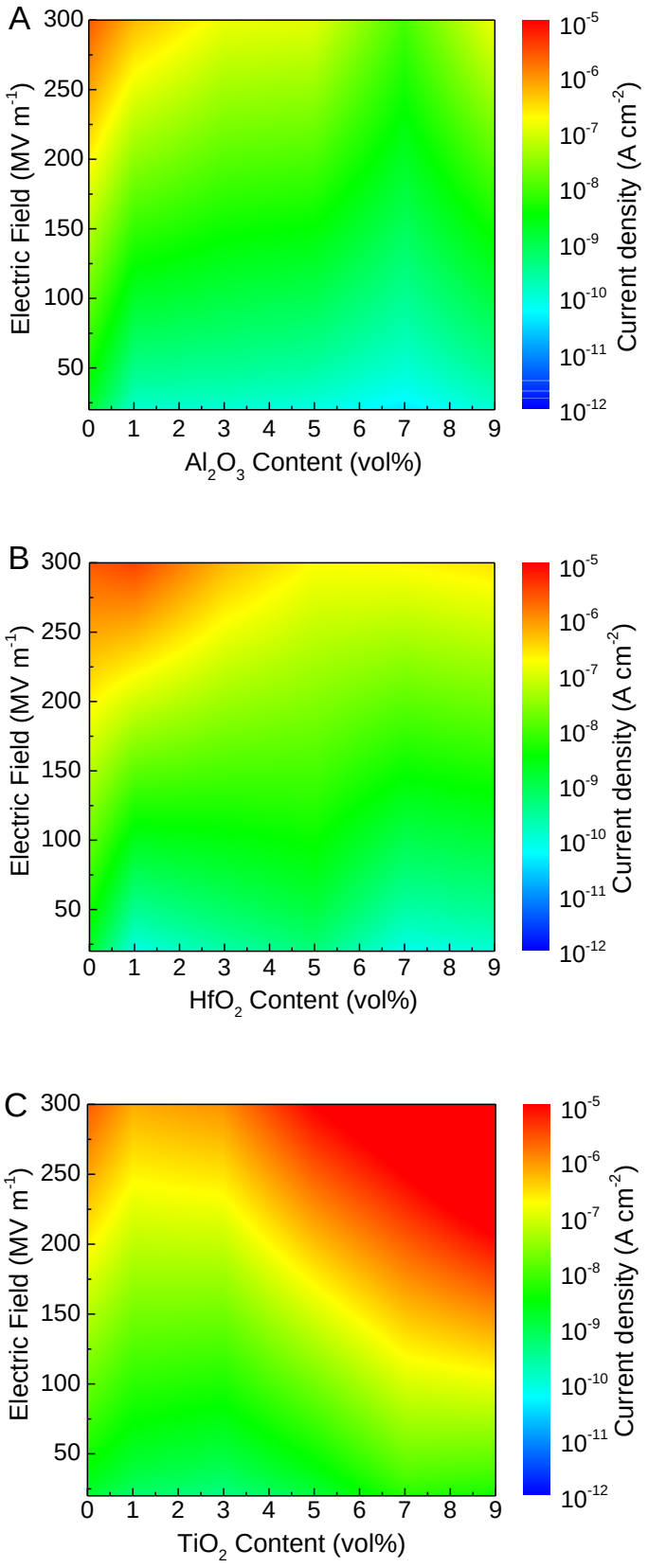

Figure 4. Simulated current density distribution as a function of **A)** Al_2O_3, **B)** HfO_2 and **C)** TiO_2 filler content and the applied electric field at 150 °C.